MATERIALS SCIENCE

Mismatched ligand density enables ordered assembly of mixed-dimensional, cross-species materials

Tongtao Li[1,2]†, Xiuyang Xia[3,4]†, Guanhong Wu[1], Qingfu Cai[2], Xuanyu Lyu[2], Jing Ning[1], Jing Wang[2], Min Kuang[1], Yuchi Yang[2], Massimo Pica Ciamarra[4], Ran Ni[3]*, Dong Yang[2]*, Angang Dong[1]*

The ordered coassembly of mixed-dimensional species—such as zero-dimensional (0D) nanocrystals and 2D microscale nanosheets—is commonly deemed impracticable, as phase separation almost invariably occurs. Here, by manipulating the ligand grafting density, we achieve ordered coassembly of 0D nanocrystals and 2D nanosheets under standard solvent evaporation conditions, resulting in macroscopic, freestanding hybrid-dimensional superlattices with both out-of-plane and in-plane order. The key to suppressing the notorious phase separation lies in hydrophobizing nanosheets with molecular ligands identical to those of nanocrystals but having substantially lower grafting density. The mismatched ligand density endows the two mixed-dimensional components with a molecular recognition–like capability, driving the spontaneous organization of densely capped nanocrystals at the interlayers of sparsely grafted nanosheets. Theoretical calculations reveal that the intercalation of nanocrystals can substantially reduce the short-range repulsions of ligand-grafted nanosheets and is therefore energetically favorable, while subsequent ligand-ligand van der Waals attractions induce the in-plane order and kinetically stabilize the laminate superlattice structure.

INTRODUCTION

Colloidal assembly allows combining distinct building blocks into one entity with precise structural control over multiple length scales (*1*–*7*). Many existing works on multicomponent ordered self-assembly have focused on colloidal nanocrystals (NCs) (*8*–*11*), mainly because of the ready access to various NC building blocks (*12*, *13*). As one of the most notable examples, coassembly of two different-sized NCs has led to binary superlattices with a rich array of structures (*14*–*22*). As the field of colloidal assembly continues to advance, there is an increasing need to integrate mixed-dimensional, cross-species materials in a predictable and controllable manner, as this provides tremendous opportunities to access emergent properties that are not otherwise presented in pure-NC assemblies (*23*–*25*). However, the phase behavior becomes enormously elusive and phase separation is commonly observed when coassembling mixed-dimensional building blocks. For instance, binary mixtures of zero-dimensional (0D) NCs and 2D microscale nanosheets (NSs) tend to undergo bulk demixing and/or microphase segregation (Fig. 1A), due to their largely different geometry and the intrinsically strong van der Waals (vdW) attractions between 2D materials (*26*, *27*). Phase separation is also entropically favored for hard spheres and hard plates, as such structural configuration can maximize the packing fraction of 0D/2D systems (*9*, *28*). One common example is displayed in the cross-sectional scanning electron microscopy (SEM) image in Fig. 1B, where phase separation occurs when drying a chloroform dispersion containing graphene oxide (GO) NSs [monolayer (1L) to few-layer thick, several hundred nanometers to a few micrometers in lateral dimension; fig. S1] and oleate-capped Fe_3O_4 NCs (~15 nm in diameter; fig. S2). Clearly, GO NSs self-stack into multilayers (MLs), whereas Fe_3O_4 NCs predominately self-assemble into bulk superlattice domains.

On the other hand, we note that 0D/2D hybrid architectures have been accessible by various approaches (*29*–*33*), yet these methods typically allow a limited structural control, giving rise to ensembles with inhomogeneous distribution of the two components in most cases. For instance, direct coassembly of NCs and NSs can easily lead to severe phase separation (*31*), whereas in situ growth methods do not allow the fine control of the structure and packing arrangement of NCs (*32*). While stacked assembly of NCs and NSs can be realized by the layer-by-layer method, this procedure is tedious and lacks the in-plane nanoscale spatial precision (*33*). In addition, the more recent electrostatic assembly method can enable the nice alternative intercalation of NCs into the interlayer of NSs, resulting in 0D/2D hybrids with homogeneous distribution of the components (*34*). Besides 0D/2D hybrids, this method also allows the fabrication of 2D/2D and 1D/2D heterostructures (*35*). Despite its versatility, electrostatic assembly applies mainly to oppositely charged components. Hence, it is highly desirable to develop previously unidentified methodologies that enable the close-packed coassembly of NCs and NSs with widely tunable compositions while preserving the precise and on-demand structural control.

Here, we report a generalized ligand-density mismatching strategy to overcome the grand challenge associated with the colloidal coassembly of NCs and NSs. Taking Fe_3O_4 NCs and GO NSs as a prototypical 0D/2D combination, we show that the substantial ligand-density difference between the two components is the key to suppressing the notorious 0D/2D phase separation, enabling hybrid-dimensional superlattices (hD-SLs) with excellent out-of-plane and in-plane order. Further theoretical calculations reveal the formation mechanism of 0D/2D hD-SLs, corroborating the vital role of ligand-density mismatching in driving the ordered coassembly of NCs and

[1]Shanghai Key Laboratory of Molecular Catalysis and Innovative Materials, Department of Chemistry, Fudan University, Shanghai 200433, China. [2]State Key Laboratory of Molecular Engineering of Polymers and Department of Macromolecular Science, Fudan University, Shanghai 200438, China. [3]Chemical Engineering, School of Chemical and Biomedical Engineering, Nanyang Technological University, 62 Nanyang Drive, Singapore 637459, Singapore. [4]Division of Physics and Applied Physics, School of Physical and Mathematical Sciences, Nanyang Technological University, 21 Nanyang Link, Singapore 637371, Singapore.
*Corresponding author. Email: r.ni@ntu.edu.sg (R.N.); yangdong@fudan.edu.cn (D.Y.); agdong@fudan.edu.cn (A.D.)
†These authors contributed equally to this work.

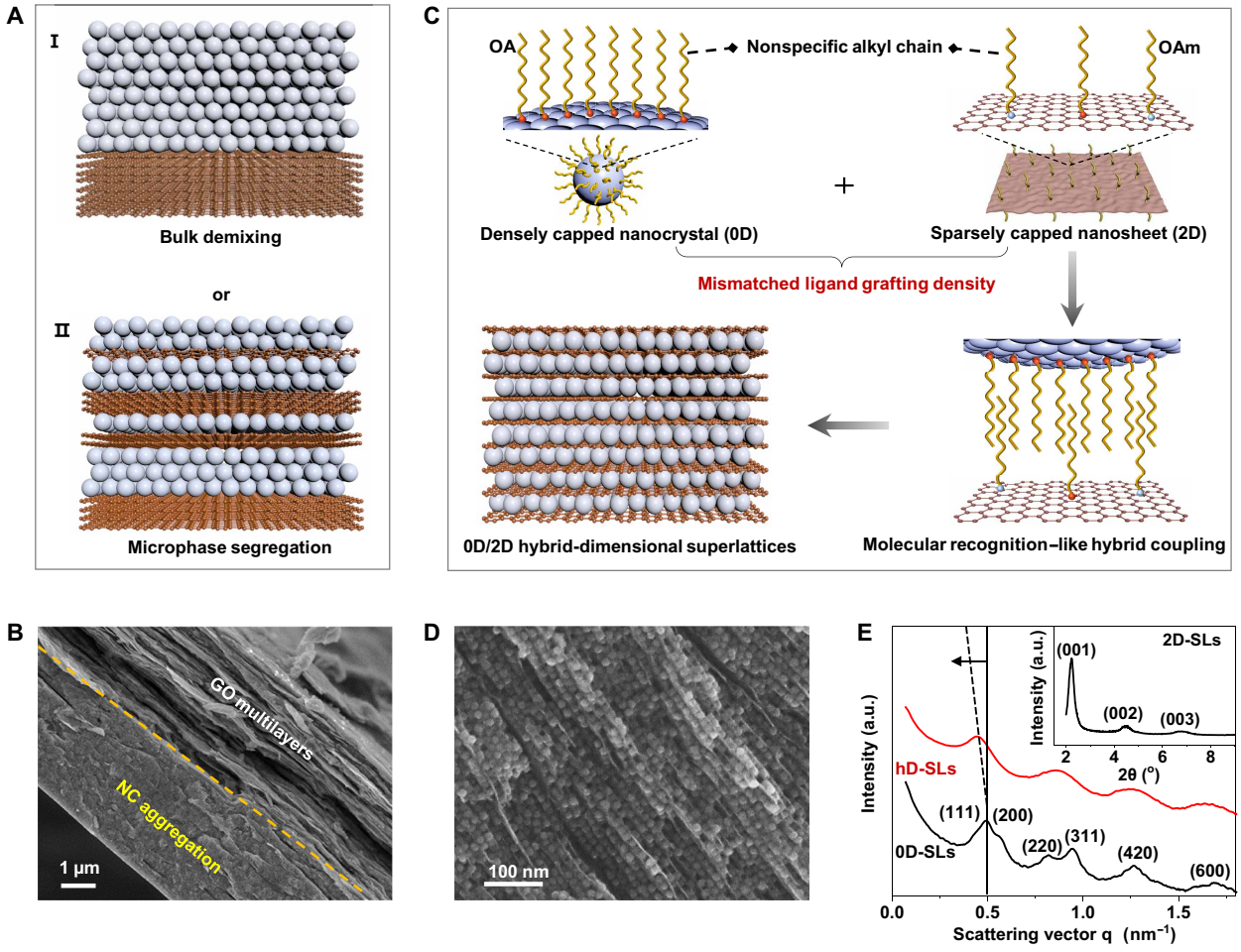

Fig. 1. Ordered coassembly of 0D NCs and 2D NSs. (**A**) Schematic illustration of conventional phase separation when coassembling 0D and 2D materials. (**B**) Cross-sectional scanning electron microscopy (SEM) image of a typical phase-separated sample when coassembling Fe_3O_4 NCs and graphene oxide (GO) NSs. (**C**) Achieving ordered coassembly of 0D and 2D materials by exploiting the concept of mismatched ligand density. OA, oleic acid; OAm, oleylamine. (**D**) Cross-sectional SEM image of 0D/2D hybrid-dimensional superlattices (hD-SLs) self-assembled from Fe_3O_4 NCs and GO NSs. (**E**) Small-angle x-ray scattering (SAXS) patterns of 0D-SLs and 0D/2D hD-SLs and low-angle x-ray diffraction pattern of 2D-SLs (inset). a.u., arbitrary units.

NSs. Benefiting from their unique structural features, such 0D/2D hD-SLs are shown to exhibit notably enhanced physiochemical properties compared with conventional pure-NC superlattices. This self-assembly method is amenable to a variety of NCs and NSs, opening a modular and controllable route for integrating mixed-dimensional, cross-species materials to construct multifunctional superstructures.

RESULTS

Self-assembly and characterization of 0D/2D hD-SLs

We note that, besides the above-mentioned thermodynamic effect, the intrinsic colloidal incompatibility between NCs and NSs may also contribute to the 0D/2D phase separation. This is due to the fact that most colloidal NSs prepared by liquid phase exfoliation (*36*), in contrast to conventional colloidal NCs (*37*), are not well dispersible in nonpolar solvents like chloroform. Therefore, a prerequisite to coassembling NCs and NSs is that the two components can be dispersed in the same solvent with comparable colloidal stability. In the light of the established merits of long alkyl chain molecular ligands in directing the assembly of various ordered superstructures (*9*, *38*), we achieve such comparable colloidal stability by modifying GO NSs with oleic acid (OA) and oleylamine (OAm) ligands commonly used for stabilizing NCs (see Materials and Methods and fig. S3). The grafting density of OA and OAm ligands on GO is modulated to be about one order of magnitude lower than that of OA ligands on Fe_3O_4 NCs (~0.4 nm^{-2} versus ~3.9 nm^{-2}, this density was defined in the text under fig. S4). Despite the low grafting density, such ligand-grafted GO NSs are well dispersible in chloroform with colloidal stability comparable to that of Fe_3O_4 NCs (fig. S5). More unexpectedly, the mismatched ligand density is found to be critical to suppressing the notorious phase separation that plagues the coassembly of mixed-dimensional building blocks. We hypothesize that, owing to the substantially different grafting density, the dense ligand chains tethered to NCs tend to penetrate the sparse ligand layer grafted onto NSs to maximize molecular interactions, thereby leading to a molecular recognition-like effect despite the absence of bonding complementarity (Fig. 1C). This is manifested by the preferential organization of densely capped NCs at GO interlayers upon solvent drying, resulting in 0D/2D hD-SLs with unprecedented out-of-plane and in-plane order without influencing the intrinsic characteristics of the two components

(Fig. 1D and fig. S6). In this hybrid architecture, each NC is separated from the adjacent NC superlattice layer by an atomically thin layer of GO. As indicated by small-angle x-ray scattering (SAXS) and low-angle x-ray diffraction, single-component superlattices self-assembled from Fe_3O_4 NCs and GO NSs (termed 0D-SLs and 2D-SLs, respectively) have a face-centered cubic and lamellar packing symmetry, respectively (Fig. 1E). In comparison, Fe_3O_4/GO hD-SLs exhibit a SAXS pattern signifying both out-of-plane and in-plane order. Meanwhile, the first scattering peak of hD-SLs shifts toward the lower angle relative to that of 0D-SLs (Fig. 1E), consistent with the enlarged interparticle spacing caused by the incorporation of GO NSs (fig. S7). The distance between adjacent GO NSs in Fe_3O_4/GO hD-SLs can be roughly determined from the SAXS pattern, which was calculated to be 14.6 nm. This distance is close to the size (15 nm) of Fe_3O_4 NCs, thus confirming that the intercalated NCs form a single layer at GO interlayers.

Owing to the delicate integration of flexible GO building blocks, resulting hD-SLs typically exist as macroscopic, freestanding laminate films (Fig. 2A and fig. S8, A and B), which is in sharp contrast to conventional pure-NC superlattices that are powders in most cases (fig. S8, C and D). Closer inspection of Fe_3O_4/GO hD-SLs reveals that Fe_3O_4 NCs assemble into 2D close-packed arrays with distinct grain boundaries conformal to the underlying GO (fig. S9). The common wrinkling in large-flake GO NSs (fig. S10) has negligible influence on the long-range ordering of NC arrays (Fig. 2, B and C). Even at the interlayers of locally folded NSs, NCs can still retain their close-packed structure (Fig. 2, D and E). To better verify the interior spatial arrangement of Fe_3O_4/GO hD-SLs, focused ion beam was used to obtain cross sections, from which close-packed NCs evenly distributed at GO interlayers are observed (Fig. 2F). Cross-sectional SEM surveys across the entire film confirm the homogeneous distribution of 1L Fe_3O_4 NCs sandwiched at GO interlayers (fig. S11).

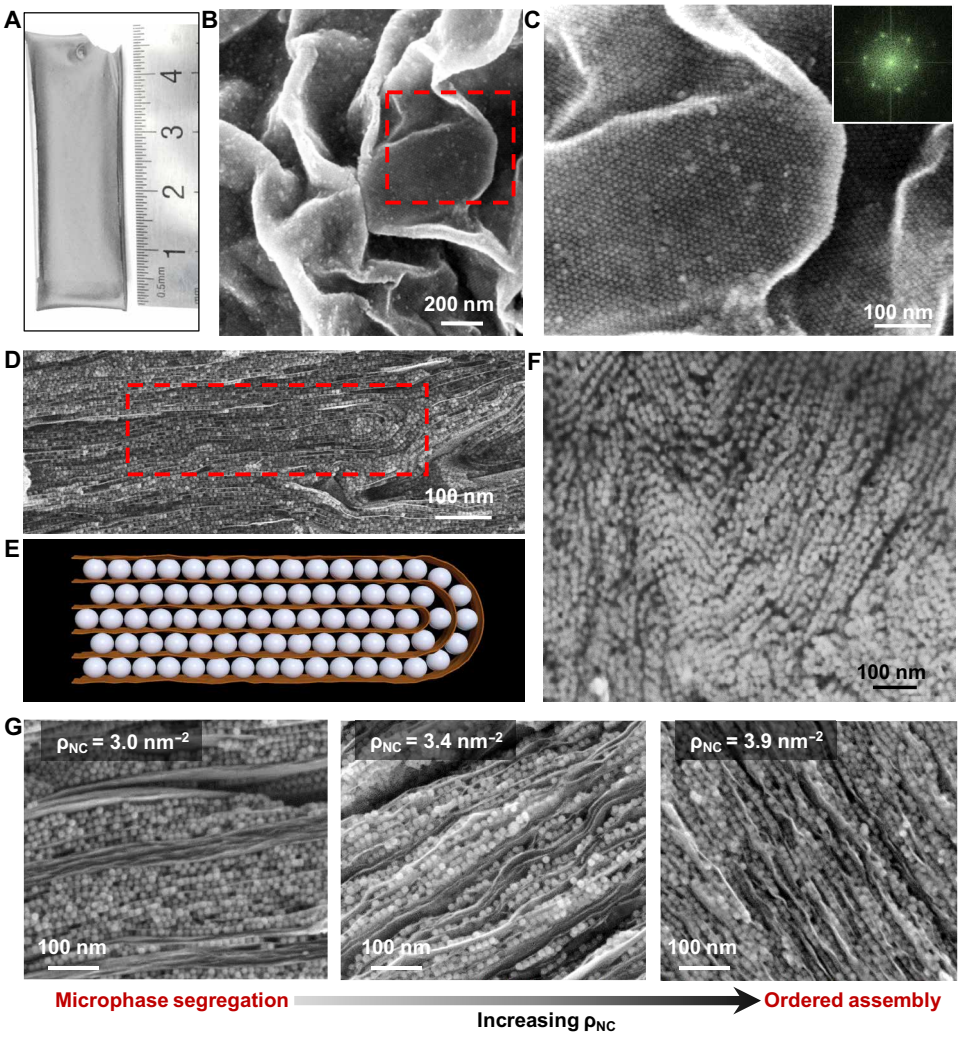

Fig. 2. Structural characterization of 0D/2D hD-SLs. (**A**) Photograph of a macroscopic Fe_3O_4/GO hD-SL laminate. (**B**) Top view SEM image of Fe_3O_4/GO hD-SL laminates. (**C**) A zoom-in taken from the region in (B) and the corresponding fast Fourier transform (inset), revealing the long-range ordered assembly of Fe_3O_4 NCs at the film surface, despite the crumpling of GO NSs. (**D**) Cross-sectional SEM image and (**E**) the corresponding schematic of Fe_3O_4/GO hD-SLs, revealing the close-packed Fe_3O_4 NCs at locally folded GO interlayers. (**F**) SEM image of focused ion beam sections. (**G**) Cross-sectional SEM images of self-assembled Fe_3O_4/GO laminates with ρ_{NC} varying from 3.0 to 3.9 nm^{-2}.

Notably, the film thickness of Fe_3O_4/GO hD-SLs can be tuned in a wide range without affecting structural order (fig. S12), simply by changing the amount of GO NSs and Fe_3O_4 NCs used for coassembly. Besides, the layer number of the intercalated Fe_3O_4 NCs can also be adjusted as ML, bilayer (2L), 1L, and even submonolayer (S1L) by tuning the ratio of the two components (fig. S13A). In addition, no apparent phase separation is observed in all cases, although the out-of-plane order of ML, 2L, and S1L laminates is inferior to that of their 1L counterparts. N_2 adsorption-desorption measurements (fig. S13B) show that the specific surface area of Fe_3O_4/GO laminates increases monotonically from 49 to 92 $m^2\ g^{-1}$ as the Fe_3O_4 layer number varies from ML to S1L. All Fe_3O_4/GO laminates have relatively uniform mesopores at ~3.7 nm regardless of the Fe_3O_4 layer number (fig. S13C). These large mesopores should be ascribed to the interstitial voids between Fe_3O_4 NCs and GO NSs, as illustrated in fig. S3D. It is also worth mentioning that the resulting Fe_3O_4/GO hD-SLs demonstrate excellent structural stability, as cooling (−196°C) or thermal (500°C) treatment has negligible influence on their global ordering (fig. S14). As expected, further increasing the temperature up to 700°C leads to the gradual sintering of the intercalated Fe_3O_4 NCs, yet the multilaminate structure of Fe_3O_4/GO hD-SLs could still be maintained.

As mentioned above, the substantially different ligand density between NCs and NSs is hypothesized to be crucial for the successful assembly of 0D/2D hD-SLs. We thereby investigate the effect of the ligand density on the structural evolution of 0D/2D systems. Although it is technically difficult to widely tune the ligand density of GO NSs, the ligand density of Fe_3O_4 NCs (ρ_{NC}) can be readily adjusted in the range of 3.0 to 3.9 nm^{-2} by repeated washing, without sacrificing their dispersibility in chloroform. As revealed by cross-sectional SEM (Fig. 2G), varying ρ_{NC} (fig. S15) while keeping the ligand density of GO at 0.4 nm^{-2} leads to distinct assembly outcomes under identical self-assembly conditions. Specifically, severe microphase segregation occurs at ρ_{NC} = 3.0 nm^{-2} where Fe_3O_4 NCs and GO NSs tend to self-assemble independently to form segregated domains. Increasing ρ_{NC} to 3.4 nm^{-2} lessens the extent of microphase segregation, while further increasing ρ_{NC} to 3.9 nm^{-2} effectively suppresses microphase segregation. These results indicate that the phase behavior of 0D/2D systems is very sensitive to the ligand density difference between NSs and NCs, provided that the comparable colloidal stability of the two types of building blocks is achieved (figs. S16 and S17).

Computational study

Tracking the coassembly process by transmission electron microscopy (TEM) reveals that Fe_3O_4 NCs and GO NSs remain largely intermixed during drying (fig. S18), suggesting that the formation of 0D/2D hD-SLs occurs at the very late stage of solvent evaporation (Fig. 3A), analogous to conventional drying-mediated assembly of pure-NC superlattices (*9*). To fundamentally understand the hybrid-assembly mechanism, we calculate pairwise interactions (βU, here $\beta = 1/k_BT$, k_B and T are the Boltzmann constant and the temperature of the system, respectively; see Materials and Methods) for two Fe_3O_4 NCs (U_{NN}), an NC and a graphene NS (U_{NG}), and two graphene NSs (U_{GG}), respectively, in both chloroform and air (i.e., after solvent drying). In our calculations, the radius of NCs, R, is fixed at 7 nm and ρ_{NC} is varied from 2.0 to 4.0 nm^{-2}, with the ligand density of graphene NSs (ρ_G) fixed at 0.4 nm^{-2}. The interaction in both environments can be estimated as the sum of vdW interaction between two nano-objects and the interaction between two ligand layers. In the first part of the interaction, the two nano-objects are mediated by a hybrid OA-solvent layer, which depends on the solvent polarity and concentration, and a pure OA layer in solvent and air, respectively. In the second part of the interaction, due to the different mobility and the volume fraction of ligands, the forms of interactions between two ligand layers in solvent and air are also different.

In good solvents like chloroform, osmotic and entropic effects dominate the effective interactions due to the fully swollen ligand layers (*9*). As a result, all components experience short-range repulsions that are consistent with the thickness of ligand layers (figs. S19, A to C, and S20, A to C). However, our calculations show that the repulsive energy between two ligand-grafted NSs is far higher than that between an NS and an NC regardless of ρ_{NC} (Fig. 3B). Therefore, when the 0D/2D system is densified caused by solvent evaporation, NCs have the tendency to undergo intercalation along with the stacking alignment of graphene NSs (Fig. 3, A and I), because such an arrangement can significantly reduce the repulsion between two ligand-grafted NSs and is therefore energetically favorable.

The spontaneous intercalation of NCs at NS interlayers is the first step toward establishing the out-of-plane order. With further solvent drying, the configuration of stretched ligands is stabilized by the stronger ligand-ligand vdW attraction (*9*). The vdW interaction between two nano-objects is weak enough to be neglected when the equilibrium separation distance, which corresponds to the minimum effective interaction, is larger than 1 nm (figs. S19 and S20). Instead, the vdW attraction or elastic repulsion between two ligand layers will dominate the effective interactions, producing different assembly outcomes depending strongly on ρ_{NC}. Specifically, NCs at low ligand coverages ($\rho_{NC} \leq 3.0\ nm^{-2}$) experience pronounced molecular interpenetration, such that U_{NN} attraction is much higher than U_{NG} attraction (Fig. 3, C and D, and fig. S19, D and E). As a result, NCs would preferentially self-assemble rather than coassemble with NSs, thereby leading to microphase segregation (Fig. 3AII, left). For NCs with high ligand coverages ($\rho_{NC} > 3.0\ nm^{-2}$), U_{NN} attraction decreases with increasing ρ_{NC} and turns out to be lower than U_{NG} attraction at $\rho_{NC} > \sim 3.5\ nm^{-2}$ (Fig. 3, C and D). This is because the ligand shell of NCs becomes too dense to allow efficient molecular interpenetration (*39*), which is particularly true for NCs at $\rho_{NC} = 4.0\ nm^{-2}$ where elastic repulsion dominates U_{NN} interactions (fig. S20D). In contrast, ligand-ligand vdW attraction continues to govern U_{NG} interactions even at ρ_{NC} = 4.0 nm^{-2} (Fig. 3D and fig. S20E). This result can be understood by considering that the sparse ligand layer tethered to graphene NSs can still penetrate the dense ligand shell of NCs (Fig. 1C). Therefore, with the increasingly greater competition of U_{NG} attraction, NCs having dense ligand shells tend to coassemble with NSs to inhibit microphase segregation (Fig. 3AII, right). Because of the dense packing and the intense attraction between ligand layers, the vibrational entropy difference between NCs' self-assembly and coassembly with graphene NSs is negligible. Hence, a critical ρ_{NC}, below which coassembly is no longer observable, occurs when the minimum of U_{NG} $\left(U_{NG}^{min}\right)$ is equal to that of U_{NN} $\left(U_{NN}^{min}\right)$. Figure 3E shows the plots of U_{NG}^{min} and U_{NN}^{min} as a function of ρ_{NC} while fixing ρ_G at 0.4 nm^{-2}, where the cross-point between the two curves is the critical ρ_{NC}. One can see that the critical ρ_{NC} is ~3.6 nm^{-2}, which agrees quantitatively with the experimental observation (Fig. 2G).

It is worth mentioning that, due to the intrinsically large graphene-graphene vdW contribution, U_{GG} attraction is considerably higher than U_{NG} attraction regardless of ρ_{NC} (figs. S19F and S20F), which should favor the self-stacking of graphene NSs thermodynamically. However, to squeeze the intercalated NCs out of graphene layers,

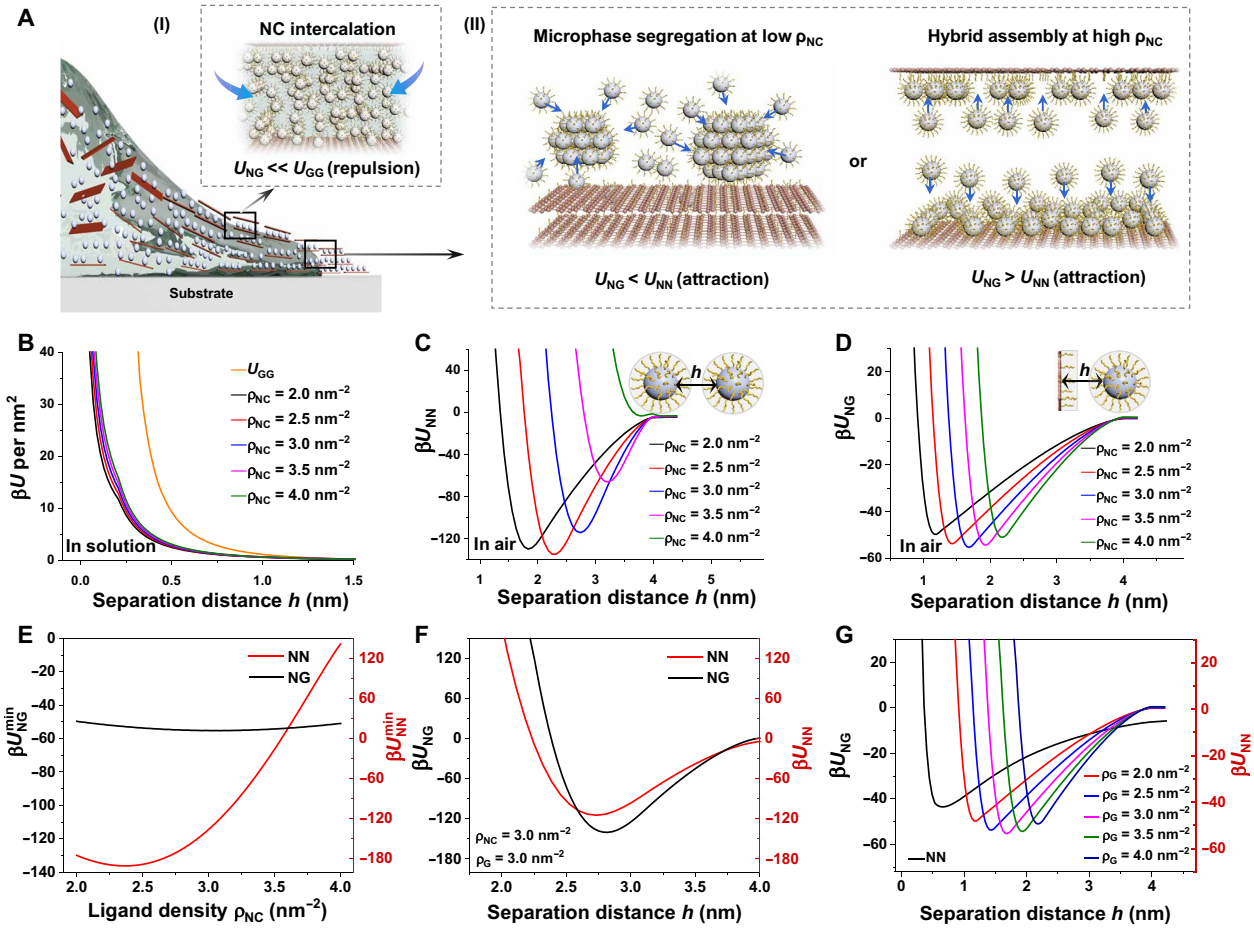

Fig. 3. Ligand density–dependent formation of 0D/2D hD-SLs. (**A**) Schematics of the drying-mediated assembly of NCs and NSs, showing the influence of ligand coverage of NCs on 0D/2D assembly behaviors. (**B**) Calculated interaction energy per unit area as a function of the separation distance (*h*) between an NC and a graphene NS in chloroform. Orange trace is the interaction between two graphene NSs. Calculated ligand density–dependent (**C**) U_{NN} and (**D**) U_{NG} interactions in air. (**E**) Plots of the minimum U_{NG} and U_{NN} interactions as a function of ligand density ρ_{NC} while fixing ρ_G at 0.4 nm^{-2}. (**F**) Calculated U_{NG} and U_{NN} interactions in air when the two mixed-dimensional components have the same ligand density at 3.0 nm^{-2}. (**G**) Calculated U_{NG} and U_{NN} interactions in air for graphene NSs with various ρ_G while fixing ligand density ρ_{NC} at 0.4 nm^{-2}. NN, nanocrystal-nanocrystal; NG, nanocrystal-graphene; GG, graphene-graphene.

the system must pay a large energetic penalty. To illustrate this, we calculate the ligand-ligand vdW attraction between NCs and NSs, which is ~−50 k_BT per particle at ρ_{NC} = 4.0 nm^{-2}. We speculate that such a large vdW attraction is sufficiently strong to restrict the escape of NCs from graphene layers, thus kinetically stabilizing the 0D/2D laminate structure. In this context, sandwiching monolayer NCs between two NSs is more favored, because such an arrangement can maximize ligand-ligand vdW interactions between the two mixed-dimensional components. It should also be noted that, in addition to driving the intercalation of NCs in solution, the soft ligand layer tethered to NSs is also beneficial for establishing the in-plane order subsequently, presumably through a self-assembly process resembling molecular epitaxy (*40*). We hypothesize that before the complete solvent evaporation, the in-plane organization of the intercalated NCs proceeds before their coassembly with GO NSs. Entropy should be the main force driving the in-plane close-packed assembly of NCs considering the weak NC-NC interactions, while the ligand layer tethered to GO NSs could facilitate the movement of NCs at interlayers by providing steric repulsions. Upon the complete solvent evaporation, the strong ligand-ligand vdW interactions between NCs and NSs start to dominate the 0D/2D coassembly and eventually stabilize the hybrid structure.

The above calculation results, in good agreement with experimental observations shown in Fig. 2G, suggest that the substantially different ligand density between of NCs and NSs plays a vital role in suppressing phase separation. In this mechanism, the NCs to be intercalated should have high ligand density, as NCs with lower ligand density tend to self-assemble, thus disturbing their hybrid assembly with NSs. Meanwhile, NSs should have comparatively low ligand density to induce the intercalation and fixation of NCs at interlayers. In this context, the densely capped NCs behave like "adhesives" gluing together the sparsely grafted NSs through molecular interpenetration (fig. S21). To further illustrate the importance of ligand-density mismatching for achieving cooperative hybrid assembly, we calculate U_{NN} and U_{NG} interactions when the ligand density of NCs and NSs is identical. Our calculations predict that U_{NN} and U_{NG} attractions are comparable under these conditions (Fig. 3F and fig. S22). We surmise that, with similar ligand density, the self-assembly of NCs competes with their coassembly with NSs, which will inevitably lead to microphase segregation. On the other hand, reversing the relation

between the mismatched ligand density of NCs and NSs, i.e., higher ρ_G and lower ρ_{NC}, also induces comparable U_{NN} and U_{NG} attractions theoretically (fig. S23). Figure 3G shows the calculated U_{NG} and U_{NN} interactions in air for graphene NSs with various ρ_G while fixing ρ_{NC} at 0.4 nm^{-2}. One can clearly see that U_{NN} will compete with U_{NG} under this situation, and, as a result, microphase segregation is predicted to be inevitable. Experimentally, one can reasonably expect that NCs with such a low ρ_{NC} would be colloidally unstable when dispersed in chloroform due to the weak ligand repulsions, which favors the self-organization of NCs and could lead to the phase separation as well.

Notably, besides the short-range vdW interactions, the contribution of the long-range electrostatic interactions in driving the coassembly of NCs and NSs was also investigated. The results indicate that the electrostatic interaction can only play a very minor role in driving the 0D/2D coassembly, because both the ligand-grafted NCs and NSs bear only a small amount of surface charges (fig. S24). This is also consistent with previous work dealing with the self-assembly of organically stabilized colloidal nanostructures (*41*, *42*), where the electrostatic contribution is usually excluded as the main driving force.

Compositional engineering of 0D/2D hD-SLs

It is also noteworthy that the size and composition of NCs and NSs play a minor role in calculating pairwise interactions (fig. S25), suggesting that the coassembly of various 0D and 2D building blocks is possible by exploiting the concept of ligand-density mismatching. Replacing 15-nm Fe_3O_4 NCs with cubic Fe_3O_4 (19 nm), octahedral MnO (15 nm), and cubic Cu (73 nm) NCs while keeping GO has no apparent influence on the hybrid-assembly behavior, resulting in 0D/2D hD-SLs with diverse NC compositions (Fig. 4, A to C). To further demonstrate the versatility of the approach, the coassembly of Fe_3O_4 NCs with different 2D building blocks was also investigated (Fig. 4D). We first select the more rigid MXene ($Ti_3C_2T_x$, a few hundred nanometers in lateral dimension) as the 2D building block (*4*), which is modified with OAm with a ligand coverage density of ~0.5 nm^{-2}. Analogous to GO NSs, coassembly of MXene NSs and Fe_3O_4 NCs under the same solvent-drying conditions produces high-quality 0D/2D hD-SLs, in which the alternating alignment of the two mixed-dimensional components can be well established by cross-sectional SEM, TEM, and elemental mapping (Fig. 4, E to G). Furthermore, when taking titanium oxide NSs modified with OA as the 2D building block (*43*), similar 0D/2D hD-SLs can also be achieved

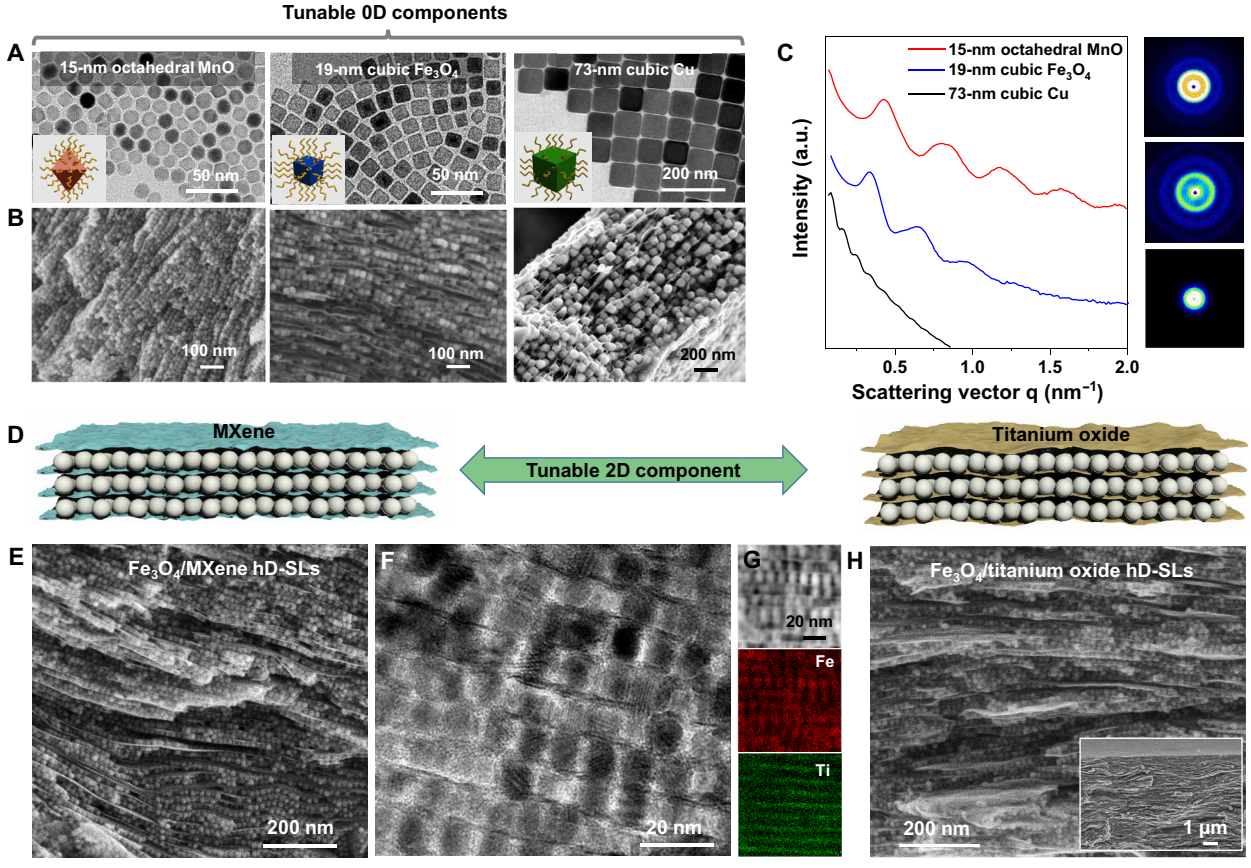

Fig. 4. Generality of the 0D/2D coassembly approach. (**A**) TEM images of 15-nm octahedral MnO, 19-nm cubic Fe_3O_4, and 73-nm cubic Cu NCs. Insets show the schematics of the corresponding NCs. (**B**) Cross-sectional SEM images and (**C**) SAXS patterns of 0D/2D hD-SLs self-assembled from GO NSs and various NCs shown in (A). (**D**) Schematic showing the tunable 2D component of hD-SLs. Cross-sectional (**E**) SEM, (**F**) TEM images, and (**G**) scanning TEM image and corresponding elemental mapping of hD-SLs self-assembled from Fe_3O_4 NCs and MXene NSs. (**H**) Cross-sectional SEM images of hD-SLs self-assembled from Fe_3O_4 NCs and titanium oxide NSs. Inset shows the corresponding low-magnification image.

upon coassembly with Fe_3O_4 NCs (Fig. 4H). These results clearly demonstrate that the composition of the two mixed-dimensional components can be independently tuned, thus offering a modular route to create multidimensional metamaterials with user-specific functionalities.

DISCUSSION

In summary, we have demonstrated by both experiments and theoretical calculations that ligand density mismatching can be exploited to effectively suppress the phase separation during colloidal coassembly of NCs and NSs without encoding any specific bonding complementarity. Our experimental and computational results underscore the significance of the molecular-level understanding of the role of ligand-ligand interactions responsible for driving cooperative assembly of multicomponent building blocks that are drastically different in geometry and surface chemistry. Given the generality of the approach, we anticipate that deterministic multidimensional metamaterials with emergent physiochemical properties can be realized through judicious selection of mixed-dimensional, cross-species building blocks.

MATERIALS AND METHODS

Synthesis of colloidal NCs

Spherical Fe_3O_4 NCs (15 nm)

In a typical synthesis procedure, iron oleate (36 g) and OA (8.6 g) were dissolved in 1-ctadecene (ODE; 180 g) in a 500-ml three-neck flask. The resulting solution was degassed at 120°C and subsequently heated up to 320°C under N_2 and kept at this temperature for 1 hour before cooling down to room temperature. Fe_3O_4 NCs were separated and purified by centrifugation with methanol and ethanol as antisolvents. The precipitated Fe_3O_4 NCs were redispersed in chloroform with a concentration of ~50 mg ml^{-1}.

Cubic Fe_3O_4 NCs (19 nm)

Iron oleate (18 g), sodium oleate (3.1 g), and OA (5.5 g) were dissolved in ODE (40 g) in a 500-ml three-neck flask. The resulting solution was degassed at 120°C and subsequently heated up to 320°C under N_2 and held at this temperature for 2 hours. The purification and dispersion were conducted similarly to their spherical counterparts.

Octahedral MnO NCs (15 nm)

Manganese oleate (4.96 g) and OA (1.12 g) were dissolved in ODE (40 g) in a 100-ml three-neck flask. The resulting mixture was degassed at 120°C for 1 hour, then heated up to 320°C under N_2 and held at this temperature for 3 hours. The purification and dispersion were conducted similarly to their Fe_3O_4 counterparts.

Cubic Cu NCs (73 nm)

CuBr (86 mg) and trioctylphosphine oxide (194 mg) were dissolved into OAm (7 ml) in a three-necked flask by vigorous stirring at 80°C for 15 min. Then, the resulting solution was heated up to 260°C quickly and held at this temperature for 2.5 hours. The purification and dispersion were conducted similarly to their Fe_3O_4 counterparts.

Preparation of ligand-grafted NSs

In a typical procedure for modifying GO NSs, a mixture containing GO NSs (80 mg), hexane (30 ml), and OAm (300 μl) was ultrasonically treated for 10 min at room temperature. Into the above mixture, 300 μl of OA ligands (300 μl) was injected followed by ultrasonic treatment for another 10 min. After that, the ligand-grafted GO NSs were separated by centrifugation with ethanol (90 ml) as antisolvents. The precipitated GO NSs were redispersed in 20 ml of chloroform to form stable colloidal dispersions with a concentration of 4 mg ml^{-1}.

To obtain the ligand-grafted MXene ($Ti_3C_2T_x$) NSs, we first prepared the delaminated MXene ($Ti_3C_2T_x$) by selective etching of Al from Ti_3AlC_2 with HF. Then, a similar modification procedure was conducted using OAm as ligands to enable stable colloidal dispersions in chloroform. To access the ligand-grafted titanium oxide NSs, we synthesized layered titanate ($H_{1.07}Ti_{1.73}O_4{\cdot}H_2O$) and delaminated it in a tetrabutylammonium hydroxide solution (*43*), followed by a modification procedure similar to their GO counterparts.

Self-assembly of 0D/2D hD-SLs

0D/2D hD-SLs were prepared based on a solvent evaporation–induced self-assembly process under ambient conditions. In a typical procedure for constructing Fe_3O_4/GO hD-SLs, a chloroform solution containing Fe_3O_4 NCs and ligand-grafted GO NSs with appropriate ratios was placed in a porcelain combustion boat, which was then covered by a glass slide. The subsequent evaporation of chloroform triggered the coassembly of Fe_3O_4 NCs and GO NSs, resulting in 0D/2D hD-SLs as macroscopic multilaminates after the complete solvent evaporation. The layer number of Fe_3O_4 NCs sandwiched between GO NSs can be precisely tuned by varying the ratio of the two components.

SUPPLEMENTARY MATERIALS

Supplementary material for this article is available at https://science.org/doi/10.1126/sciadv.abq0969

REFERENCES AND NOTES

1. G. M. Whitesides, B. Grzybowski, Self-assembly at all scales. *Science* **295**, 2418–2421 (2002).
2. S. C. Glotzer, M. J. Solomon, Anisotropy of building blocks and their assembly into complex structures. *Nat. Mater.* **6**, 557–562 (2007).
3. Y. Nagaoka, R. Tan, R. P. Li, H. Zhu, D. Eggert, Y. M. A. Wu, Y. Z. Liu, Z. W. Wang, O. Chen, Superstructures generated from truncated tetrahedral quantum dots. *Nature* **561**, 378–382 (2018).
4. G. Wu, T. Li, Z. Wang, M. Li, B. Wang, A. Dong, Molecular ligand-mediated assembly of multicomponent nanosheet superlattices for compact capacitive energy storage. *Angew. Chem. Int. Ed.* **59**, 20628–20635 (2020).
5. C. Avci, I. Imaz, A. Carne-Sanchez, J. A. Pariente, N. Tasios, J. Perez-Carvajal, M. I. Alonso, A. Blanco, M. Dijkstra, C. Lopez, D. Maspoch, Self-assembly of polyhedral metal-organic framework particles into three-dimensional ordered superstructures. *Nat. Chem.* **10**, 78–84 (2017).
6. T. Wang, J. Zhuang, J. Lynch, O. Chen, Z. Wang, X. Wang, D. LaMontagne, H. Wu, Z. Wang, Y. C. Cao, Self-assembled colloidal superparticles from nanorods. *Science* **338**, 358–363 (2012).
7. T. Li, B. Wang, J. Ning, W. Li, G. Guo, D. Han, B. Xue, J. Zou, G. Wu, Y. Yang, A. Dong, D. Zhao, Self-assembled nanoparticle supertubes as robust platform for revealing long-term, multiscale lithiation evolution. *Matter* **1**, 976–987 (2019).
8. C. Yan, T. Wang, A new view for nanoparticle assemblies: From crystalline to binary cooperative complementarity. *Chem. Soc. Rev.* **46**, 1483–1509 (2017).
9. M. A. Boles, M. Engel, D. V. Talapin, Self-assembly of colloidal nanocrystals: From intricate structures to functional materials. *Chem. Rev.* **116**, 11220–11289 (2016).
10. C. Gadiyar, A. Loiudice, F. D'Ambra, E. Oveisi, D. Stoian, P. Iyengar, L. Castilla-Amoros, V. Mantella, R. Buonsanti, Nanocrystals as precursors in solid-state reactions for size- and shape-controlled polyelemental nanomaterials. *J. Am. Chem. Soc.* **142**, 15931–15940 (2020).
11. T. Udayabhaskararao, T. Altantzis, L. Houben, M. Coronado-Puchau, J. Langer, R. Popovitz-Biro, L. M. Liz-Marzan, L. Vukovic, P. Kral, S. Bals, R. Klajn, Tunable porous nanoallotropes prepared by post-assembly etching of binary nanoparticle superlattices. *Science* **358**, 514–518 (2017).
12. Y. W. Jun, J. S. Choi, J. Cheon, Shape control of semiconductor and metal oxide nanocrystals through nonhydrolytic colloidal routes. *Angew. Chem. Int. Ed.* **45**, 3414–3439 (2006).
13. J. Park, J. Joo, S. G. Kwon, Y. Jang, T. Hyeon, Synthesis of monodisperse spherical nanocrystals. *Angew. Chem. Int. Ed.* **46**, 4630–4660 (2007).

14. F. X. Redl, K. S. Cho, C. B. Murray, S. O'Brien, Three-dimensional binary superlattices of magnetic nanocrystals and semiconductor quantum dots. *Nature* **423**, 968–971 (2003).
15. E. V. Shevchenko, D. V. Talapin, N. A. Kotov, S. O'Brien, C. B. Murray, Structural diversity in binary nanoparticle superlattices. *Nature* **439**, 55–59 (2006).
16. D. V. Talapin, E. V. Shevchenko, M. I. Bodnarchuk, X. C. Ye, J. Chen, C. B. Murray, Quasicrystalline order in self-assembled binary nanoparticle superlattices. *Nature* **461**, 964–967 (2009).
17. A. G. Dong, J. Chen, P. M. Vora, J. M. Kikkawa, C. B. Murray, Binary nanocrystal superlattice membranes self-assembled at the liquid-air interface. *Nature* **466**, 474–477 (2010).
18. I. Cherniukh, G. Raino, T. Stoferle, M. Burian, A. Travesset, D. Naumenko, H. Amenitsch, R. Erni, R. F. Mahrt, M. I. Bodnarchuk, M. V. Kovalenko, Perovskite-type superlattices from lead halide perovskite nanocubes. *Nature* **593**, 535–542 (2021).
19. K. C. Elbert, W. Zygmunt, T. Vo, C. M. Vara, D. J. Rosen, N. M. Krook, S. C. Glotzer, C. B. Murray, Anisotropic nanocrystal shape and ligand design for co-assembly. *Sci. Adv.* **7**, eabf9402 (2021).
20. X. Ye, C. Zhu, P. Ercius, S. N. Raja, B. He, M. R. Jones, M. R. Hauwiller, Y. Liu, T. Xu, A. P. Alivisatos, Structural diversity in binary superlattices self-assembled from polymer-grafted nanocrystals. *Nat. Commun.* **6**, 10052 (2015).
21. O. Chen, L. Riedemann, F. Etoc, H. Herrmann, M. Coppey, M. Barch, C. T. Farrar, J. Zhao, O. T. Bruns, H. Wei, P. Guo, J. Cui, R. Jensen, Y. Chen, D. K. Harris, J. M. Cordero, Z. W. Wang, A. Jasanoff, D. Fukumura, R. Reimer, M. Dahan, R. K. Jain, M. G. Bawendi, Magneto-fluorescent core-shell supernanoparticles. *Nat. Commun.* **5**, 5093 (2014).
22. Y. Yang, B. Wang, X. Shen, L. Yao, L. Wang, X. Chen, S. Xie, T. Li, J. Hu, D. Yang, A. Dong, Scalable assembly of crystalline binary nanocrystal superparticles and their enhanced magnetic and electrochemical properties. *J. Am. Chem. Soc.* **140**, 15038–15047 (2018).
23. H. X. Lin, L. Chen, D. Y. Liu, Z. C. Lei, Y. Wang, X. S. Zheng, B. Ren, Z. X. Xie, G. D. Stucky, Z. Q. Tian, Constructing two-dimensional nanoparticle arrays on layered materials inspired by atomic epitaxial growth. *J. Am. Chem. Soc.* **137**, 2828–2831 (2015).
24. F. Qiu, J. R. Edison, Z. Preisler, Y. F. Zhang, G. Li, A. Pan, C. H. Hsu, T. M. Mattox, P. Ercius, C. Song, K. Bustillo, M. A. Brady, E. W. Zaia, S. Jeong, J. B. Neaton, S. Du, S. Whitelam, J. J. Urban, Design rules for self-assembly of 2D nanocrystal/metal-organic framework superstructures. *Angew. Chem. Int. Ed.* **57**, 13172–13176 (2018).
25. V. Liljestrom, A. Ora, J. Hassinen, H. T. Rekola, Nonappa, M. Heilala, V. Hynninen, J. J. Joensuu, R. H. A. Ras, P. Torma, O. Ikkala, M. A. Kostiainen, Cooperative colloidal self-assembly of metal-protein superlattice wires. *Nat. Commun.* **8**, 671 (2017).
26. D. V. Talapin, J. S. Lee, M. V. Kovalenko, E. V. Shevchenko, Prospects of colloidal nanocrystals for electronic and optoelectronic applications. *Chem. Rev.* **110**, 389–458 (2010).
27. J. Shen, Y. Zhu, H. Jiang, C. Li, 2D nanosheets-based novel architectures: Synthesis, assembly and applications. *Nano Today* **11**, 483–520 (2016).
28. M. Schmidt, H. Lowen, Phase diagram of hard spheres confined between two parallel plates. *Phys. Rev. E* **55**, 7228–7241 (1997).
29. D. Wang, R. Kou, D. Choi, Z. Yang, Z. Nie, J. Li, L. V. Saraf, D. Hu, J. Zhang, G. L. Graff, J. Liu, M. A. Pope, I. A. Aksay, Ternary self-assembly of ordered metal oxide-graphene nanocomposites for electrochemical energy storage. *ACS Nano* **4**, 1587–1595 (2010).
30. E. S. Cho, A. M. Ruminski, S. Aloni, Y. S. Liu, J. H. Guo, J. J. Urban, Graphene oxide/metal nanocrystal multilaminates as the atomic limit for safe and selective hydrogen storage. *Nat. Commun.* **7**, 10804 (2016).
31. J. K. Lee, K. B. Smith, C. M. Hayner, H. H. Kung, Silicon nanoparticles-graphene paper composites for Li ion battery anodes. *Chem. Commun.* **46**, 2025–2027 (2010).
32. Q. Xue, Z. Pei, Y. Huang, M. Zhu, Z. Tang, H. Li, Y. Huang, N. Li, H. Zhang, C. Zhi, Mn_3O_4 nanoparticles on layer-structured Ti_3C_2 MXene towards the oxygen reduction reaction and zinc-air batteries. *J. Mater. Chem. A* **5**, 20818–20823 (2017).
33. T. Lee, S. H. Min, M. Gu, Y. K. Jung, W. Lee, J. U. Lee, D. G. Seong, B.-S. Kim, Layer-by-layer assembly for graphene-based multilayer nanocomposites: Synthesis and applications. *Chem. Mater.* **27**, 3785–3796 (2015).
34. K. Ament, N. Kowitsch, D. Hou, T. Gotsch, J. Krohnert, C. J. Heard, A. Trunschke, T. Lunkenbein, M. Armbruster, J. Breu, Nanoparticles supported on sub-nanometer oxide films: Scaling model systems to bulk materials. *Angew. Chem. Int. Ed.* **60**, 5890–5897 (2021).
35. L. Zhang, M. Jaroniec, Strategies for development of nanoporous materials with 2D building units. *Chem. Soc. Rev.* **49**, 6039–6055 (2020).
36. V. Nicolosi, M. Chhowalla, M. G. Kanatzidis, M. S. Strano, J. N. Coleman, Liquid exfoliation of layered materials. *Science* **340**, e1226419 (2013).
37. M. A. Boles, D. Ling, T. Hyeon, D. V. Talapin, The surface science of nanocrystals. *Nat. Mater.* **15**, 141–153 (2016).
38. T. Kudernac, S. Lei, J. A. Elemans, S. De Feyter, Two-dimensional supramolecular self-assembly: Nanoporous networks on surfaces. *Chem. Soc. Rev.* **38**, 402–421 (2009).
39. T. K. Patra, H. Chan, P. Podsiadlo, E. V. Shevchenko, S. Sankaranarayanan, B. Narayanan, Ligand dynamics control structure, elasticity, and high-pressure behavior of nanoparticle superlattices. *Nanoscale* **11**, 10655–10666 (2019).
40. T. Li, B. Xue, B. Wang, G. Guo, D. Han, Y. Yan, A. Dong, Tubular monolayer superlattices of hollow Mn_3O_4 nanocrystals and their oxygen reduction activity. *J. Am. Chem. Soc.* **139**, 12133–12136 (2017).
41. X. Ye, J. Chen, C. B. Murray, Polymorphism in self-assembled AB_6 binary nanocrystal superlattices. *J. Am. Chem. Soc.* **133**, 2613–2620 (2011).
42. F. Zhang, R. Liu, Y. Wei, J. Wei, Z. Yang, Self-assembled open porous nanoparticle superstructures. *J. Am. Chem. Soc.* **143**, 11662–11669 (2021).
43. Y. Zhou, K. Jiang, Z. Zhao, Q. Li, R. Ma, T. Sasaki, F. Geng, Giant two-dimensional titania sheets for constructing a flexible fiber sodium-ion battery with long-term cycling stability. *Energy Stor. Mater.* **24**, 504–511 (2020).
44. J. Park, K. J. An, Y. S. Hwang, J. G. Park, H. J. Noh, J. Y. Kim, J. H. Park, N. M. Hwang, T. Hyeon, Ultra-large-scale syntheses of monodisperse nanocrystals. *Nat. Mater.* **3**, 891–895 (2004).
45. J. N. Israelachvili, *Intermolecular and Surface Forces* (Academic Press, 2011).
46. B. Derjaguin, Untersuchungen über die Reibung und Adhäsion, IV. *Kolloid-Zeitschrift* **69**, 155–164 (1934).
47. M. A. Boles, D. V. Talapin, Self-assembly of tetrahedral CdSe nanocrystals: Effective "patchiness" via anisotropic steric interaction. *J. Am. Chem. Soc.* **136**, 5868–5871 (2014).
48. Z. H. Ni, H. M. Wang, J. Kasim, H. M. Fan, T. Yu, Y. H. Wu, Y. P. Feng, Z. X. Shen, Graphene thickness determination using reflection and contrast spectroscopy. *Nano Lett.* **7**, 2758–2763 (2007).
49. B. Vincent, J. Edwards, S. Emmett, A. Jones, Depletion flocculation in dispersions of sterically-stabilised particles ("soft spheres"). *Colloids Surf.* **18**, 261–281 (1986).
50. L. A. Wijenayaka, M. R. Ivanov, C. M. Cheatum, A. J. Haes, Improved parametrization for extended derjaguin, landau, verwey, and overbeek predictions of functionalized Gold nanosphere stability. *J. Phys. Chem. C* **119**, 10064–10075 (2015).
51. A. J. Worthen, V. Tran, K. A. Cornell, T. M. Truskett, K. P. Johnston, Steric stabilization of nanoparticles with grafted low molecular weight ligands in highly concentrated brines including divalent ions. *Soft Matter* **12**, 2025–2039 (2016).
52. L. Salem, Attractive forces between long saturated chains at short distances. *J. Chem. Phys.* **37**, 2100–2113 (1962).
53. F. W. DelRio, C. Jaye, D. A. Fischer, R. F. Cook, Elastic and adhesive properties of alkanethiol self-assembled monolayers on gold. *Appl. Phys. Lett.* **94**, 131909 (2009).
54. S. Verma, D. Pravarthana, One-pot synthesis of highly monodispersed ferrite nanocrystals: Surface characterization and magnetic properties. *Langmuir* **27**, 13189–13197 (2011).
55. H. Yun, X. Y. Liu, T. Paik, D. Palanisamy, J. Kim, W. D. Vogel, A. J. Viescas, J. Chen, G. C. Papaefthymiou, J. M. Kikkawa, M. G. Allen, C. B. Murray, Size- and composition-dependent radio frequency magnetic permeability of iron oxide nanocrystals. *ACS Nano* **8**, 12323–12337 (2014).
56. P. Xiong, R. Z. Ma, N. Sakai, L. Nurdiwijayanto, T. Sasaki, Unilamellar metallic MoS_2/graphene superlattice for efficient sodium storage and hydrogen evolution. *ACS Energy Lett.* **3**, 997–1005 (2018).

Acknowledgments

Funding: This work was supported by the National Key Research and Development Program of China (2020YFB1505803), NSFC (22025501, 21872038, 21733003, 51773042, and 51973040), the Shanghai International Science and Technology Cooperation Project (21520713800), the Foshan Science and Technology Innovation Program (2017IT100121), and the Academic Research Fund Tier 1 grant from the Singapore Ministry of Education (RG59/21). **Author contributions:** A.D. and D.Y. supervised the project, conceived the idea, and wrote the paper. T.L. conceived the idea, conducted the experiments, and wrote the paper. R.N., M.P.C., and X.X. directed and conducted theoretical calculations. G.W. helped in the synthesis of MXene nanosheets. Q.C., X.L., and J.N. assisted in SEM and TGA characterizations. J.W., M.K., and Y.Y. helped in the synthesis of nanocrystals and figure preparation. All authors discussed the results and commented on the manuscript. **Competing interests:** The authors declare that they have no competing interests. **Data and materials availability:** All data needed to evaluate the conclusions in the paper are present in the paper and/or the Supplementary Materials. Codes used for the theoretical calculations are available on Zenodo at https://doi.org/10.5281/zenodo.6546592.

Submitted 17 March 2022
Accepted 16 May 2022
Published 1 July 2022
10.1126/sciadv.abq0969